Supporting Information

A RhNiP/rGO hybrid for efficient catalytic hydrogen generation from alkaline solution of hydrazine

Xiaoqiong Du, Shiyi Tan, Ping Cai, Wei Luo* and Gongzhen Cheng

College of Chemistry and Molecular Sciences, Wuhan University, Wuhan, Hubei 430072, P. R. China, Tel.: +86-27-68752366

*Corresponding author. *E-mail addresses*: wluo@whu.edu.cn.

Experimental Section

Chemicals and materials: All chemicals were commercial and used without further purification. Nickel chloride hexahydrate ($NiCl_2$•$6H_2O$, Sinopharm Chemical Reagent Co., Ltd., ≥99%), Rhodium chloride hydrate ($RhCl_3$•$3H_2O$, Wuhan Greatwall Chemical Co., Ltd., >99%), hydrazine monohydrate (N_2H_4•H_2O, TCI Shanghai Co., Ltd., >98%), sodium hypophosphite (NaH_2PO_2, Aladdin Co., Ltd., >99%), sodium borohydride ($NaBH_4$, Sinopharm Chemical Reagent Co., Ltd., >96%), potassium permanganate ($KMnO_4$, Shanghai Chemic Co., Ltd, ≥99.5%), hydrogen peroxide (H_2O_2, Sinopharm Chemical Reagent Co., Ltd, ≥30%), phosphoric acid (H_3PO_4, Sinopharm Chemical Reagent Co., Ltd, AR), sulfuric acid (H_2SO_4, Sinopharm Chemical Reagent Co., Ltd, 95~98%), graphite power (Sinopharm Chemical Reagent Co., Ltd, ≥99.85%) were used as received. Ultrapure water was used as the reaction solvent.

Preparation of RhNiP/rGO catalysts: GO (Graphene oxide) was prepared according to the modified Hummers method [*ACS Nano*, 2010, **4**, 4806]. In a typical experiment, 10 mg GO and different amounts of NaH_2PO_2 (0 mmol, 0.1 mmol, 0.2 mmol, 0.3 mmol and 0.4 mmol) were dispersed in 2 mL of water kept in a two-necked round-bottom flask. Ultrasonication was required to get a uniform dispersion. 0.8 mL rhodium chloride solution (0.1 mol L^{-1}) and 0.2

mL nickel chloride solution (0.1 mol L^{-1}) was added into the flask. The resulting mixture was then reduced by 2 mL of aqueous solution containing 37.8mg $NaBH_4$ and a certain amount of NaOH with vigorous stirring at 298 K. The process of hydrogen generation from alkaline solution of hydrazine is carried at 323 K. One neck was connected to a gas burette to monitor the volume of the gas evolution, and the other for the introduction of hydrazine monohydrate (0.1 mL, 1.96 mmol). A water bath was used to control the temperature of the reaction solution at 298 K. The gas released during the reaction was passed through HCl solution (1.0 M) before it was measured volumetrically. The selectivity towards H_2 generation (X) can be calculated using Equation S1. The value of turnover frequency (TOF) can be calculated using Equation S2.

$$X=(3\lambda-1)/8 \qquad [\lambda=n(H_2+N_2)/n(H_2NNH_2)] \qquad \text{S1}$$

$$TOF_{initial}=\frac{P_{atm}V_{H_2}/RT}{n_{Rh+Ni}t} \qquad \text{S2}$$

Where TOFinitial is initial turnover frequency, Patm is the atmospheric pressure, V_{H2} is the volume of the generated gas when the conversion reached 50%, R is the universal gas constant, T is room temperature (298 K), n_{Rh+Ni} is the mole amount of Rh and Ni, and t is the reaction time.

The relative molar quantities of $RhCl_3$, $NiCl_2$ and NaH_2PO_2 were adjusted in this study, which are summarized in Table S1. The temperatures were varied from 298 to 323 K, to obtain the activation energy (Ea) (metal/N_2H_4•H_2O = 0.05).

Physical characterizations: Powder X-ray diffraction (XRD) patterns were measured by a Bruker D8-Advance X-ray diffractometer using Cu Kα radiation source (λ = 0.154178 nm) with a velocity of 10^o min^{-1}. Raman spectroscopy was performed with a laser micro-Raman spectrometer (Renishaw inVia, Renishaw, 532 nm excitation wavelength). The morphologies and sizes of the samples were observed by using a Tecnai G20 U-Twin transmission electron microscope (TEM) at an acceleration voltage of 200 kV and a Titan G2 60-300 Titan Probe

corrected TEM equipped with an energy dispersive X-ray detector (EDX) at an acceleration voltage of 300 kV. X-ray photoelectron spectroscopy (XPS) measurement was performed with a Thermo Fischer ESCALAB 250Xi spectrophotometer. MS of the generated gases were collected by using an Ametek Dycor mass spectrometer under Ar atmosphere. Inductively coupled plasma-atomic emission spectroscopy (ICP-AES) was performed on IRIS Intrepid II XSP. Atomic Force Microscope (AFM) images were recorded in NT-MDT system via semicontact mode. The characterization of Brunauer–Emmett–Teller (BET) surface data, which was based on N_2 adsorption/desorption isotherms at 77 K and controlled by liquid nitrogen, was measured using a Quantachrome NOVA 4200e.

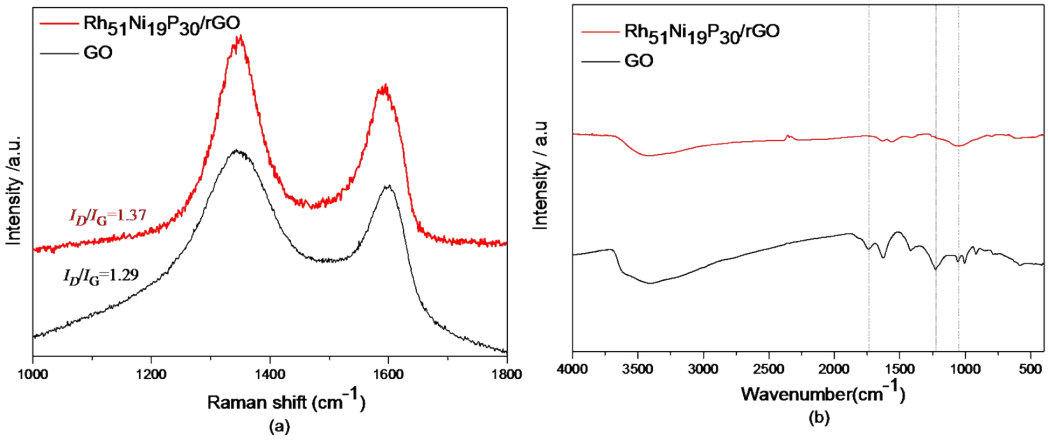

Fig. S1 (a) Raman and (b) FTIR spectra of GO and $Rh_{51}Ni_{19}P_{30}$/rGO.

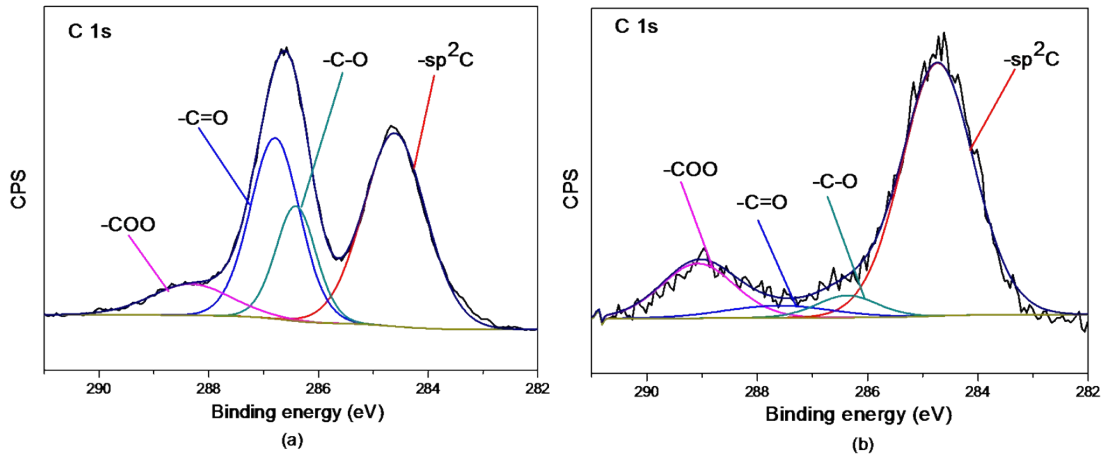

Fig. S2 XPS spectrum of C 1s for (a) GO and (b) $Rh_{51}Ni_{19}P_{30}$/rGO.

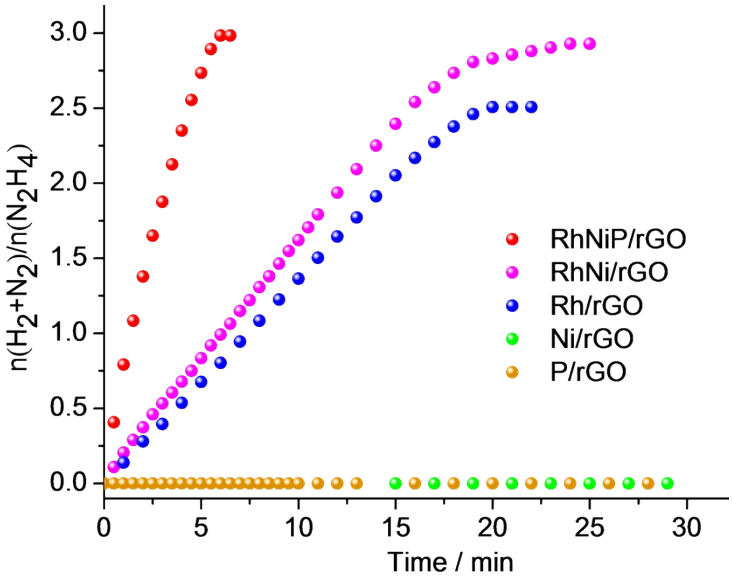

Fig. S3 Time course plots for hydrogen generation from hydrazine by RhNiP/rGO, RhNi/rGO, Rh/rGO, Ni/rGO and P/rGO at 323K.

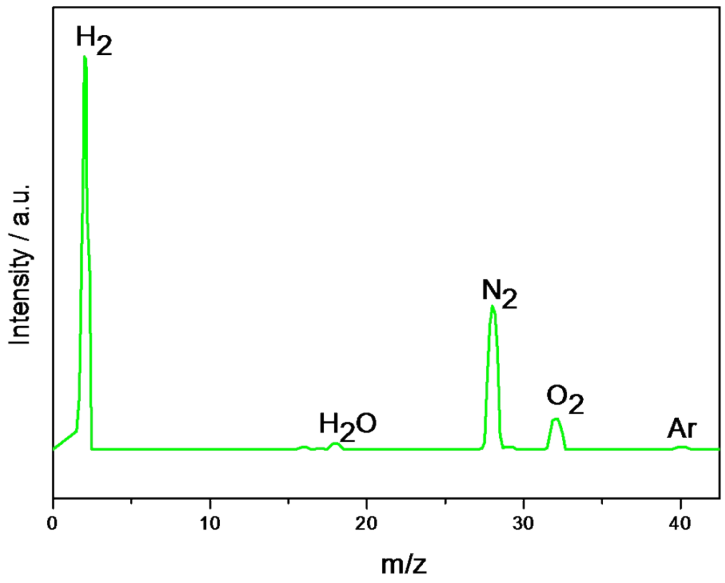

Fig. S4 Mass spectra profile of the gases released from the decomposition of hydrazine over $Rh_{51}Ni_{19}P_{30}$/rGO under an argon atmosphere at 323 K.

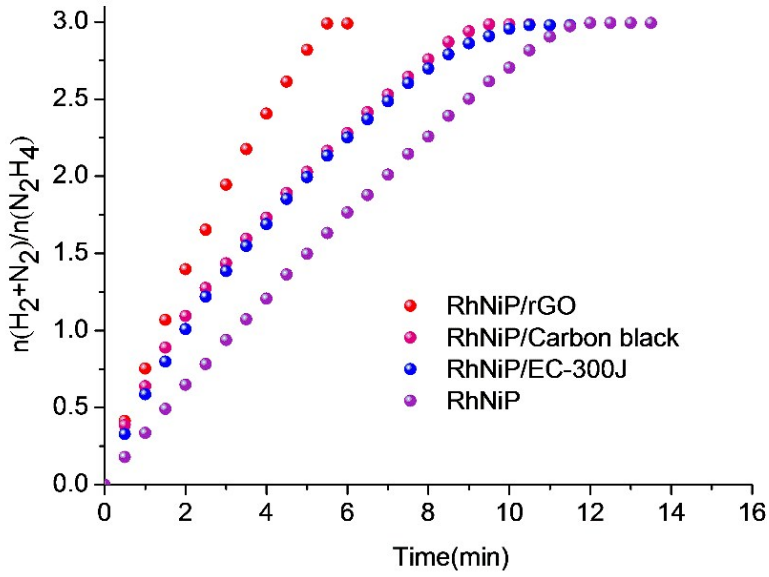

Fig. S5 Time course plots for hydrogen generation from hydrazine by $Rh_{51}Ni_{19}P_{30}$ supported on rGO, carbon black, EC-300J and no support at 323K.

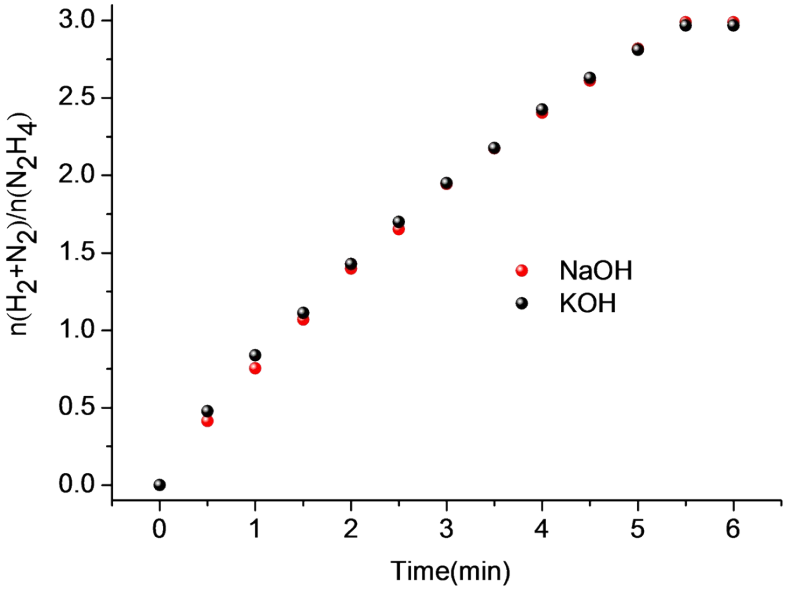

Fig. S6 Catalytic performance for hydrogen generation from alkaline solution of hydrazine catalyzed by $Rh_{51}Ni_{19}P_{30}$/rGO in aqueous NaOH or KOH solution.

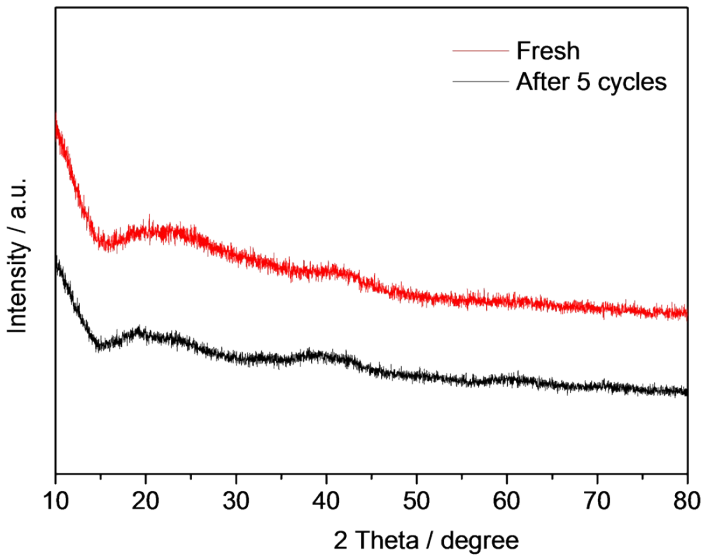

Fig. S7 Powder XRD patterns of the $Rh_{51}Ni_{19}P_{30}$/rGO for fresh (red) and after 5 cycles (black).

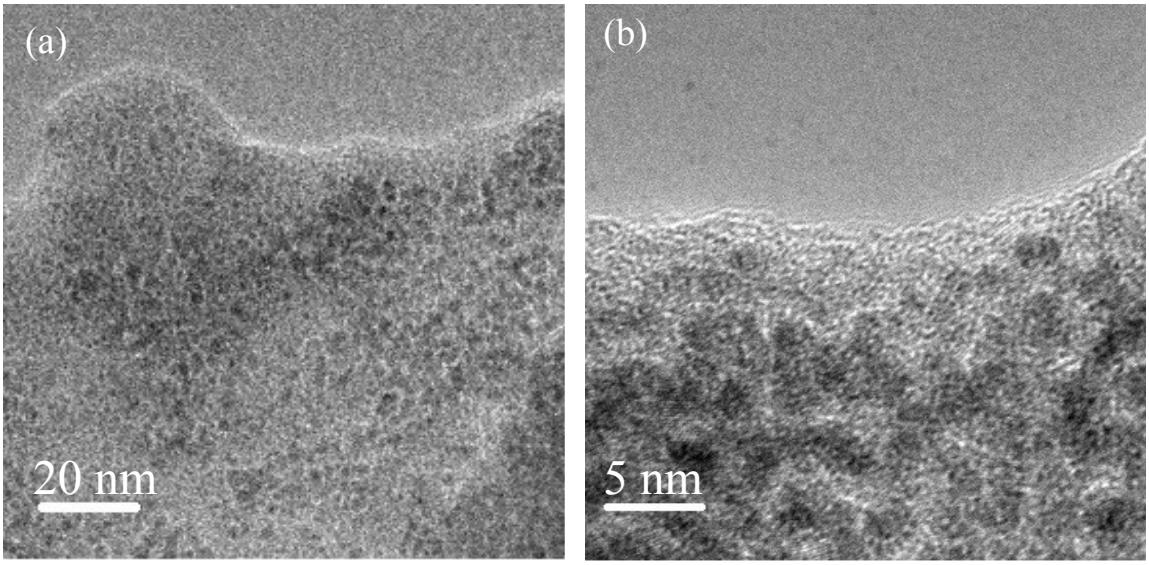

Fig. S8 TEM images of with different magnifications (a and b) of $Rh_{51}Ni_{19}P_{30}$/rGO after 5 cycles for a period of time.

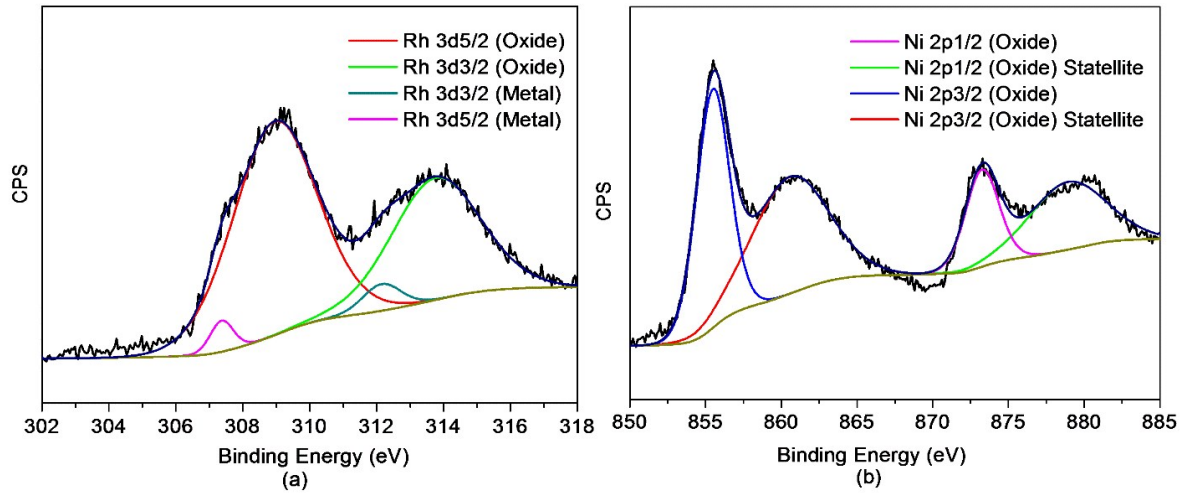

Fig. S9 XPS spectra of the (a) Rh 3d and (b) Ni 2p for $Rh_{51}Ni_{19}P_{30}$/rGO after 5 cycles for a period of time.

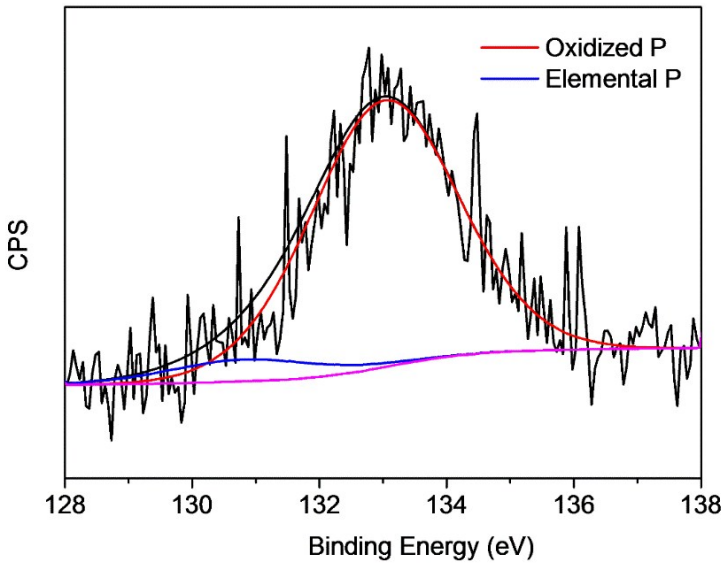

Fig. S10 XPS spectra of the P 2p for $Rh_{51}Ni_{19}P_{30}$/rGO after 5 cycles for a period of time.

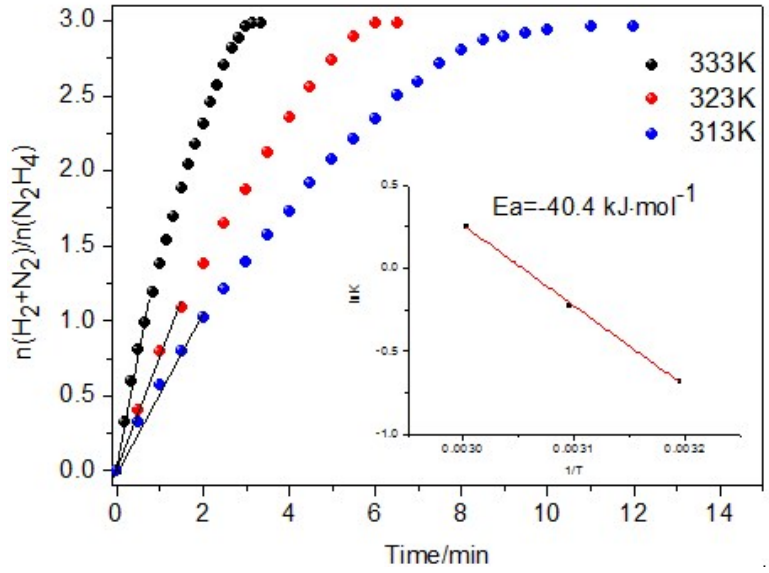

Fig. S11 Time plots for hydrogen generation from alkaline solution of hydrazine catalyzed by $Rh_{51}Ni_{19}P_{30}$/rGO at higher temperature (333K-313K) and Arrhenius plot of ln k versus 1/T during the hydrazine decomposition over $Rh_{51}Ni_{19}P_{30}$/rGO (inset).

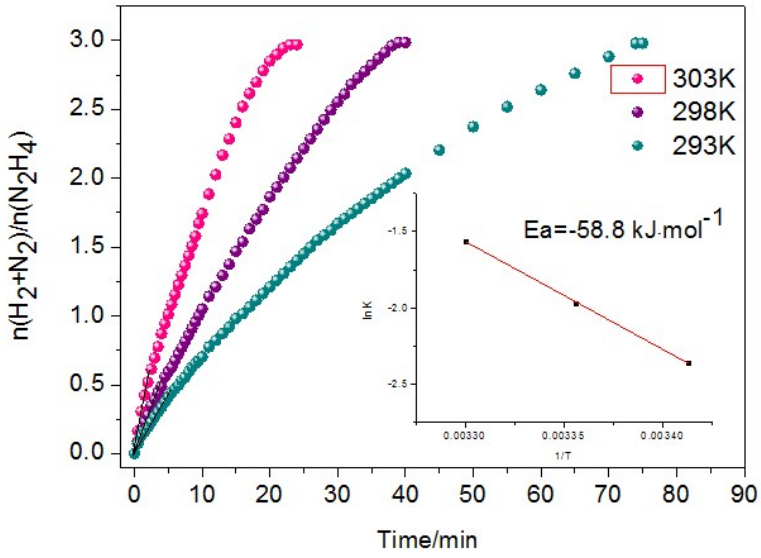

Fig. S12 (a) Time course plots for hydrogen generation from alkaline solution of hydrazine catalyzed by $Rh_{51}Ni_{19}P_{30}$/rGO at lower temperature (313K-293K) and Arrhenius plot of ln k versus 1/T during the hydrazine decomposition over $Rh_{51}Ni_{19}P_{30}$/rGO (inset).

It has been reported that hydrazine decomposition ($H_2NNH_2 \rightarrow N_2(g) + 2H_2(g)$) may proceed through different pathways and it was related to the reaction condition including reaction temperature. In one pathway, N_2 is formed intra-molecularly and not by the recombination of nitrogen species [Equation (1-5)]. (H.-L. Jiang, S. K. Singh, J.-M. Yan, X.-B. Zhang, and Q. Xu, *ChemSusChem*, 2010, **3**, 541.)

Pathway 1:

$$H_2NNH_2 \rightarrow N_2H_3^* + H^* \quad (1\text{-}1)$$

$$N_2H_3^* \rightarrow N_2H_2^* + H^* \quad (1\text{-}2)$$

$$H^* + H^* \rightarrow H_2(g) \quad (1\text{-}3)$$

$$N_2H_2^* \rightarrow N_2H^* + H^* \quad (1\text{-}4)$$

$$N_2H^* \rightarrow N_2(g) + H^* \quad (1\text{-}5)$$

$$H^* + H^* \rightarrow H_2(g) \quad (1\text{-}6)$$

In second pathway, firstly the N-N bond breaks to form the NH_2 species on the surface [Equation (2-1)], which further decomposes to nitrogen and hydrogen [Equation (2-3) and (2-4)]. It has been reported that activity energy (Ea) for one pathway is always smaller than Ea for second pathway. (Medeiros, J. E., and Valenca, G. P., Brazilian, *J. Chem. Eng*. 1998, **15**, 126.)

Pathway 2:

$$H_2NNH_2 \rightarrow NH_2^* + N^* + 2H^* \quad (2\text{-}1)$$

$$NH_2^* \rightarrow N^* + 2H^* \quad (2\text{-}2)$$

$$N^* + N^* \rightarrow N_2(g) \quad (2\text{-}3)$$

$$2H^* + 2H^* \rightarrow 2H_2(g) \quad (2\text{-}4)$$

At higher temperatures, the value of Ea is 40.4 $kJ \cdot mol^{-1}$, which indicating that the main pathway of hydrazine decomposition is one pathway. At lower temperatures, the value of Ea is 58.5 $kJ \cdot mol^{-1}$, which indicating that the second pathway of hydrazine decomposition is increasing. This the reason for H_2 evolution plots at higher temperatures is slightly faster than that at lower temperatures.

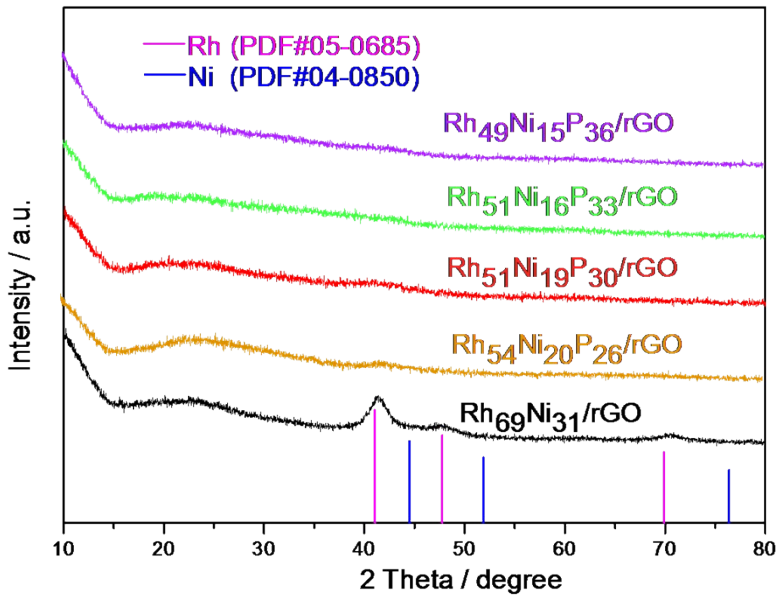

Fig. S13 Powder XRD patterns of the obtained $Rh_{69}Ni_{31}$/rGO, $Rh_{54}Ni_{20}P_{26}$/rGO, $Rh_{51}Ni_{19}P_{30}$/rGO, $Rh_{51}Ni_{16}P_{33}$/rGO and $Rh_{49}Ni_{15}P_{36}$/ rGO.

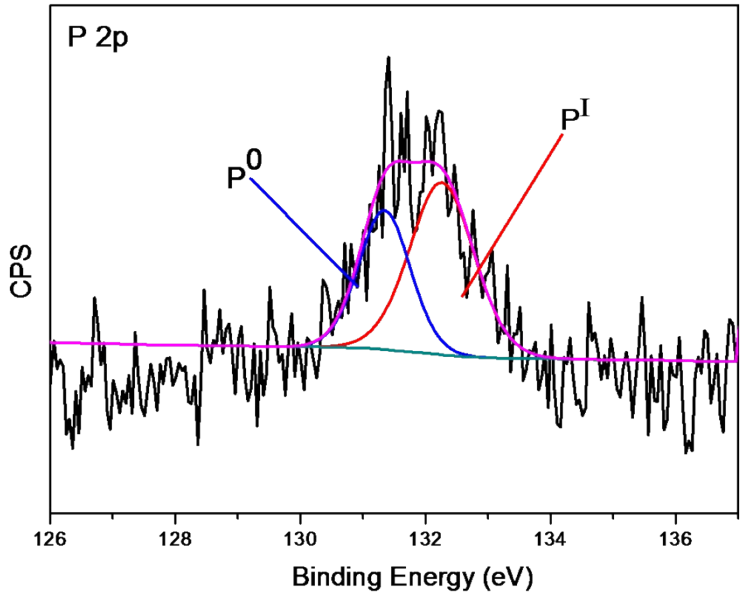

Fig. S14 XPS spectrum of the P 2p for $Rh_{51}Ni_{19}P_{30}$/rGO.

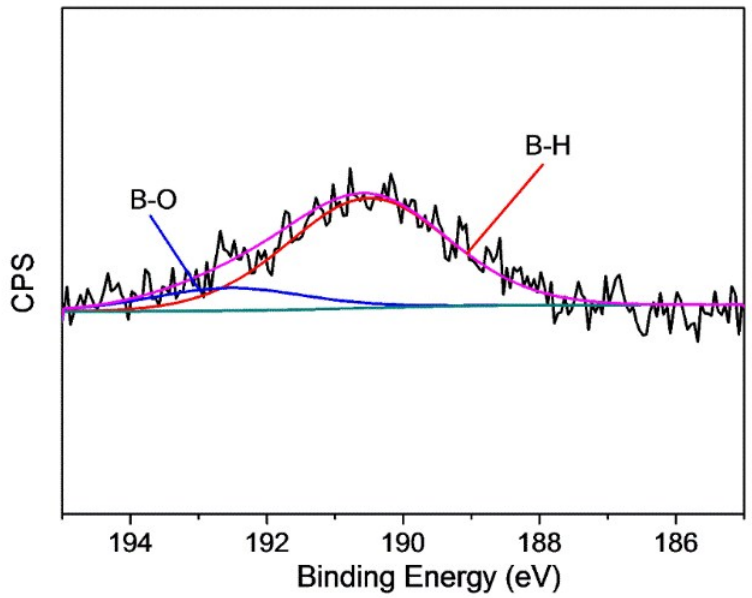

Fig. S15 B 1s XPS spectra of $Rh_{51}Ni_{19}P_{30}$/rGO.

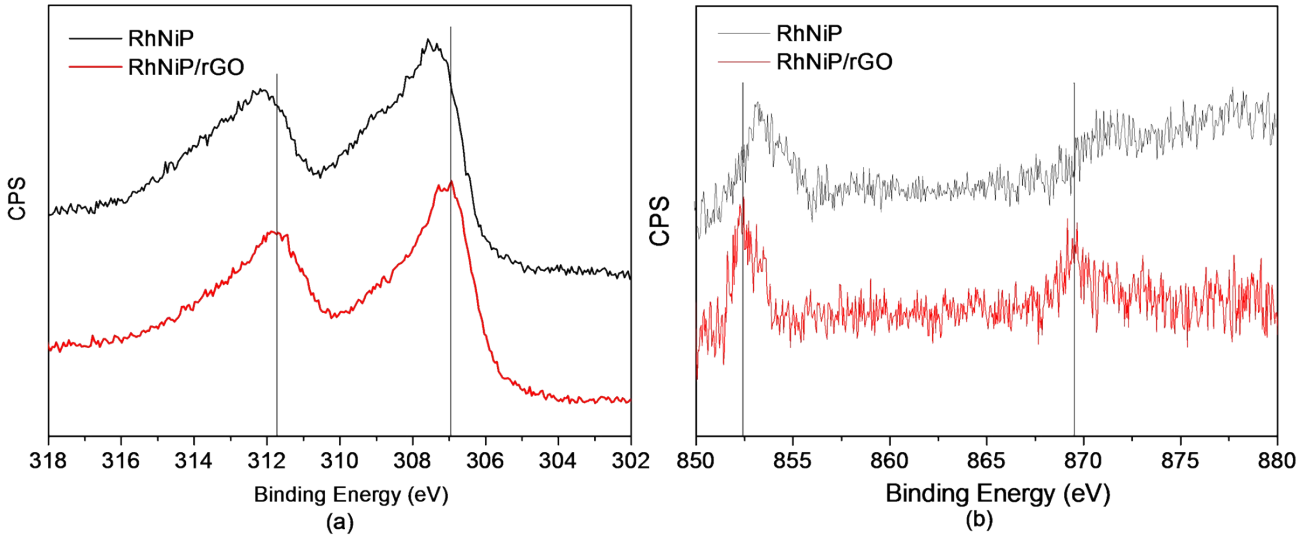

Fig. S16 Rh 3d XPS spectra (a) and Ni 2p XPS spectra of RhNiP and RhNiP/rGO after Ar sputtering.

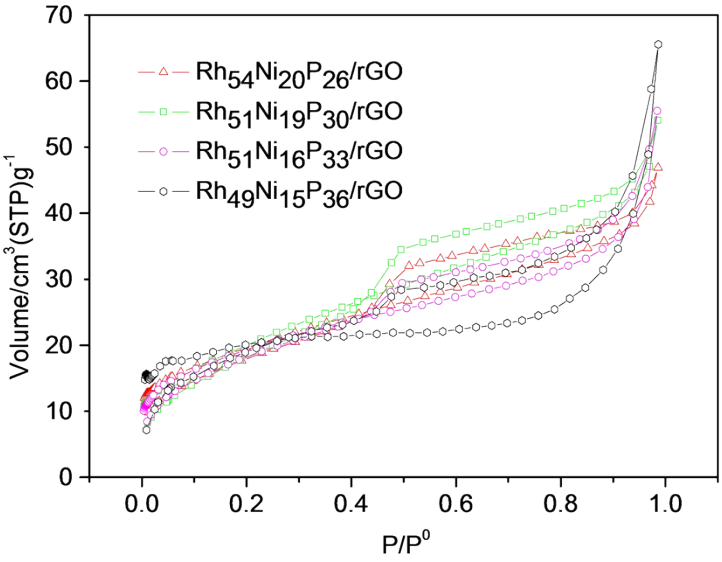

Fig. S17 N_2 adsorption/desorption isotherms for the RhNiP/rGO catalysts.

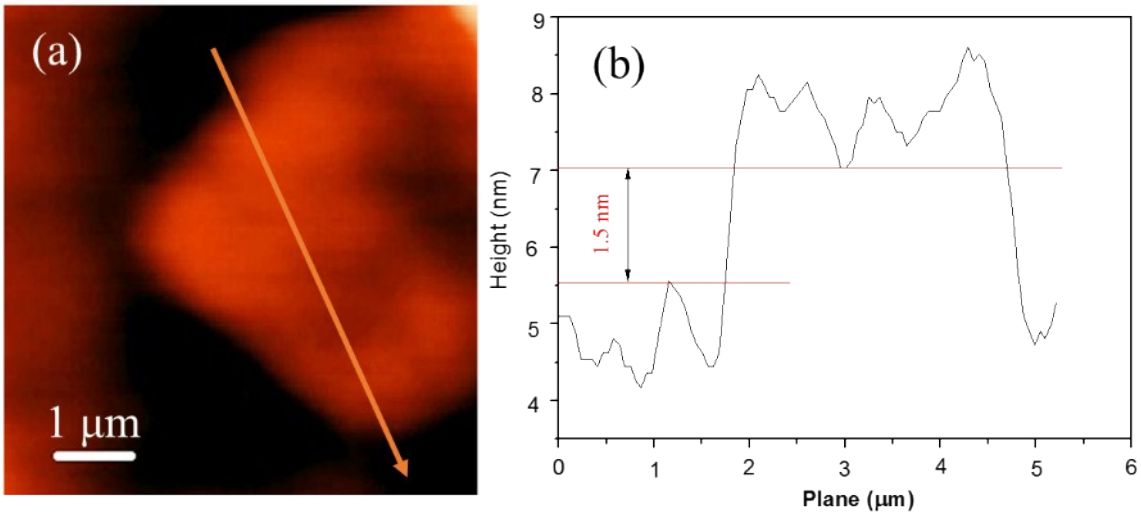

Fig.S18 AFM image (a) and the corresponding height map (b) of GO.

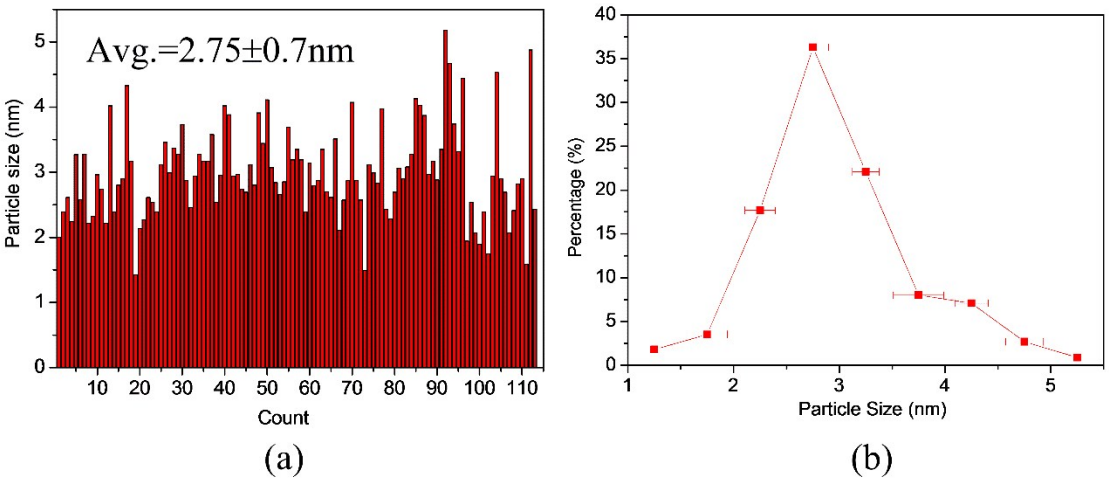

Fig. S19 Particle distribution (a, b) of $Rh_{51}Ni_{19}P_{30}$/rGO.

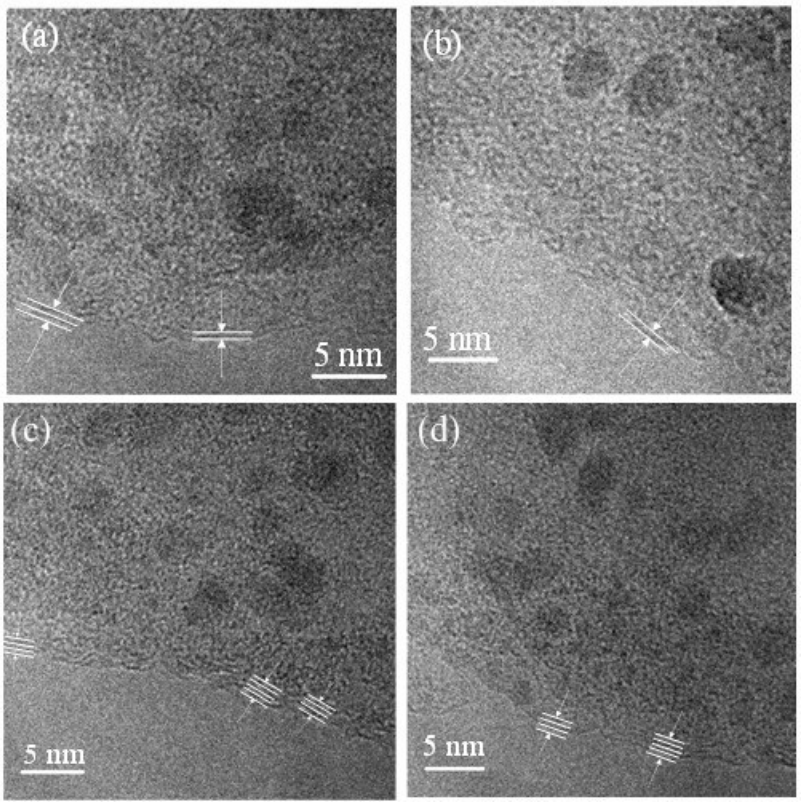

Fig. S20 TEM image of $Rh_{51}Ni_{19}P_{30}$/rGO (Note: transverse line represent the layer of GO).

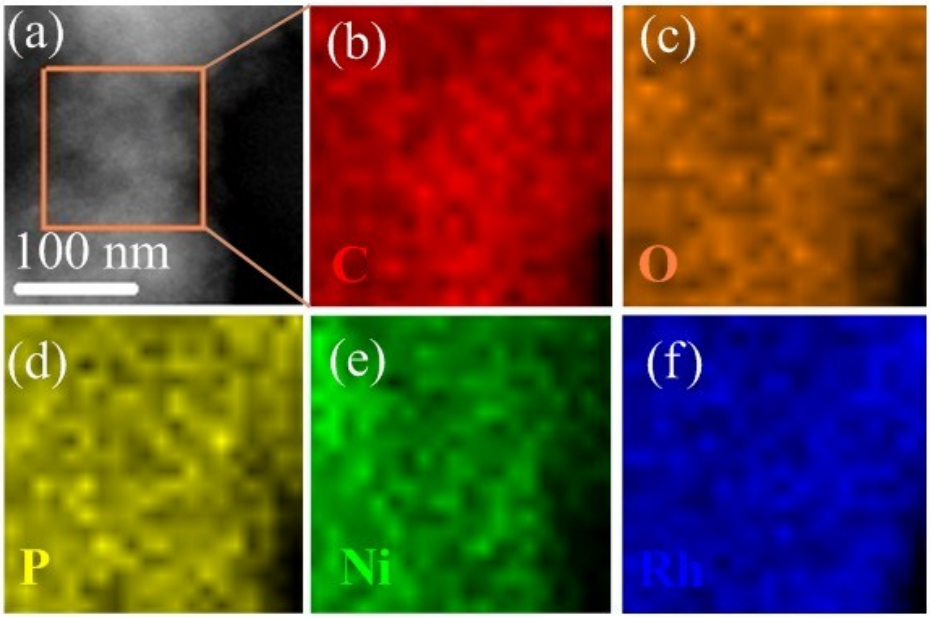

Fig. S21 HADDF-STEM and EDX mapping images of $Rh_{51}Ni_{19}P_{30}$/rGO.

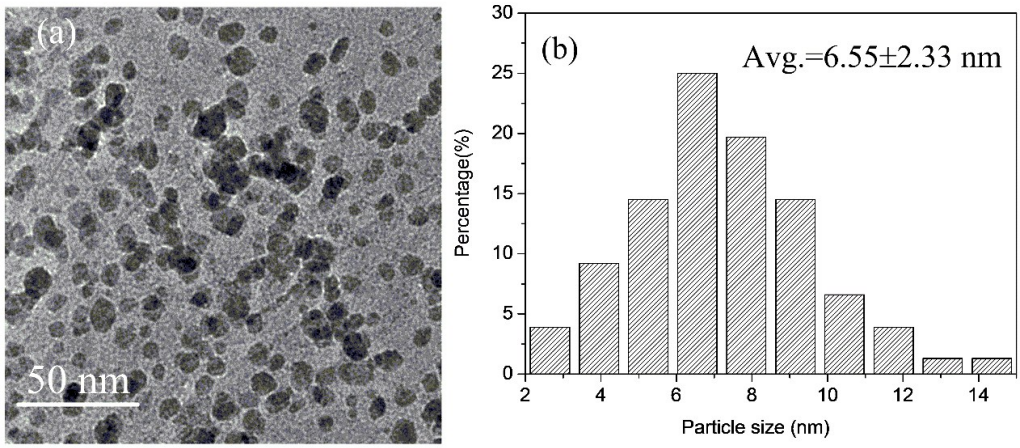

Fig. S22 (a) TEM images and (b) particle distribution of $Rh_{69}Ni_{31}$/rGO.

Table S1. Reactant molar ratios and ICP results for the synthesis of various samples.

Catalysts	Initial molar ratios			ICP results			
	$RhCl_3$	$NiCl_2$	NaH_2PO_2	Rh (wt.%)	Ni (wt.%)	P (wt.%)	Rh: Ni: P (at.%)
$Rh_{69}Ni_{31}$/rGO	0.08	0.02	0	24.82	6.47	0	69: 31: 0
$Rh_{54}Ni_{20}P_{26}$/rGO	0.08	0.02	0.1	27.41	5.64	3.96	54: 20: 26
$Rh_{51}Ni_{19}P_{30}$/rGO	0.08	0.02	0.2	24.85	5.37	4.41	51: 19: 30
$Rh_{51}Ni_{16}P_{33}$/rGO	0.08	0.02	0.3	24.56	4.35	4.79	51: 16: 33
$Rh_{49}Ni_{15}P_{36}$/rGO	0.08	0.02	0.4	24.89	4.45	5.51	49: 15: 36

Table S2 Comparison of decomposition of hydrazine over different catalysts.

Catalysts	*T* (°C)	H_2 selectivity/%	Ea ($kJ \cdot mol^{-1}$)	TOF[a] (h^{-1})	Reference
Co-B-N-H	20	100	39.9	4560	1
Ni_2B urchins	20	90.0	44.9	22.2	2
Honeycomb-like Co–B	25	41.8	54.3	756	3
Cobalt–boron spherical	25	21.3	-	320	4
Fe–B/MWCNTs	25	97.0	46.7	4032	5
$Rh_{51}Ni_{19}P_{30}$/rGO	25	100	58.8	101	This work
RhNiB	30	100	-	54.5	6
$Ni_{0.60}Pd_{0.40}$	50	82.0	-	3.80	7
$Rh_{10}Ni_{90}$	50	100	-	3.30	8
$Rh_{0.8}Ni_{0.2}$@CeO_x/rGO	50	100	58.0	211	9
$Rh_{55}Ni_{45}$/$Ce(OH)CO_3$	50	100	38.8	395	10
Ni@Ni-Pt/La_2O_3	50	100	56.2	156	11
$Ni_{66}Rh_{34}$@ZIF-8	50	100	58.1	93.3	12
$Rh_{58}Ni_{42}$@MIL-101	50	100	33.0	344	13
$Ni_{88}Pt_{12}$@MIL-101	50	100	51.3	212	14
Ni_3Rh_7/NPC-900	50	100	-	104	15
Ni_3Pt_7/rGO	50	100	49.4	277	16
$Ni_{0.6}Fe_{0.4}Mo$	50	100	50.7	28.8	17

$NiMoB/La(OH)_3$	50	100	55.1	26.7	18
$Rh_{51}Ni_{19}P_{30}/rGO$	50	100	40.4	471	This work
NiFe	70	100	-	6.3	19
$Cu@Fe_5Ni_5$	70	100	-	18.2	20

[a] The TOF values were calculated according to the original data provided by the reports.

Table S3 BET surface area of RhNiP/rGO catalysts.

Catalysts	BET surface area $cm^2 \cdot g^{-1}$
$Rh_{54}Ni_{20}P_{26}/rGO$	70.8
$Rh_{51}Ni_{19}P_{30}/rGO$	74.8
$Rh_{51}Ni_{16}P_{33}/rGO$	71.0
$Rh_{49}Ni_{15}P_{36}/rGO$	80.9

Reference

1 F. Yang, Y.Z. Li, W. Chu, C. Li and D.G. Tong, *Catal. Sci. Technol*., 2014, **4**, 3168.

2 M. Deng, S.Y. Fu, F. Yang, P. Wu and D.G. Tong, *J. Nanosci. Nanotechnol*., 2016, **16**, 2394.

3 D.G. Tong, W. Chu, P. Wu and L. Zhang, *RSC Advances*, 2012, **2**, 2369.

4 D.G. Tong, X.L. Zeng, W. Chu, D. Wang, P. Wu, *Mater. Res. Bull*., 2010, **45**, 442.

5 D.G. Tong, W. Chu, P. Wu, G.F. Gu and L. Zhang, *J. Mater. Chem. A*, 2013, **1**, 358.

6 J. Wang, W. Li, Y. R. Wen, L. Gu and Y. Zhang, *Adv. Energy Mater*., 2015, **5**, 1401879.

7 S. K. Singh, Y. Lizuka and Q. Xu, *Int. J. Hydrogen Energy*, 2011, **36**, 11794.

8 A. K. Singh, M. Yadav, K. Aranishi and Q. Xu, *Int. J. Hydrogen Energy*, 2012, **37**, 18915.

9 Z. Zhang, Z-H. Lu, H. Tan, X. Chen and Q. Yao, *J. Mater. Chem. A*, 2015, **3**, 23520.

10 J. M. Chen, Q. L. Yao, J. Zhu, X. S. Chen, Z. H. Lu, *Int. J. Hydrogen Energy*, 2016, **41**, 3946.

11 Y.-J. Zhong, H.-B. Dai, Y.-Y. Jiang, D.-M. Chen, M. Zhu, L.-X. Sun, P. Wang, *J. Power Sources*, 2015, **300**, 294.

12 B. Q. Xia, N. Cao, H. M. Dai, J. Su, X. J. Wu, W. Luo, G. Z. Cheng, *ChemCatChem,* 2014, **6**, 2549.

13 P. P. Zhao, N. Cao, W. Luo, G. Z. Cheng, *J. Mater. Chem. A,* 2015, **3**, 12468.

14 N. Cao, L. Yang, H. Dai, T. Liu, J. Su, X. Wu, W. Luo, G. Cheng, *Inorg. Chem*., 2014, **53**, 10122.

15 B. Q. Xia, K. Chen, W. Luo, G. Z. Cheng, *Nano Research*, 2015, **8**, 3472.

16 N. Cao, L. Yang, C. Du, J. Su, W. Luo, G. Cheng, *J. Mater. Chem. A*, 2014, **2**, 14344.

17 H.-L. Wang, J.-M. Yan, S.-J. Li, X.-W. Zhang, Q. Jiang, *J. Mater. Chem. A,* 2015, **3**, 121.

18 J. Zhang, Q. Kang, Z. Yang, H. Dai, D. Zhuang, P. Wang, *J. Mater. Chem. A*, 2013, **1**, 11623.

19 S. K. Singh, A. K. Singh, K. Aranishi, Q. Xu, *J. Am. Chem. Soc*., 2011, **133**, 19638.

20 J. Wang, Y. Li, Y. Zhang, *Adv. Funct. Mater*., 2014, **24**, 7073.